

www.acsami.org Research Article

MOF-Derived Bimetallic Pd—Co Alkaline ORR Electrocatalysts

Weixuan Xu, Dasol Yoon, Yao Yang, Yin Xiong, Huiqi Li, Rui Zeng, David A. Muller, and Héctor D. Abruña*





ACCESS I Metrics & More Article Recommendations Supporting Information - E_{1/2} ECSA 0.99 Mass Activity Specific Activity 0.98 100 E_{1/2} / V vs RHE В 2 nm 0.97 ⁻D °E 80 ECSA/ 0.96 0.95

ABSTRACT: The development of highly active, durable, and low-cost electrocatalysts for the oxygen reduction reaction (ORR) has been of paramount importance for advancing and commercializing fuel cell technologies. Here, we report on a novel family of Pd–Co binary alloys (Pd_xCo, x = 1-6) embedded in bimetallic organic framework (BMOF)-derived polyhedral carbon supports. BMOF-derived Pd₃Co, annealed at 300–400 °C, exhibited the most promising ORR activity among the family of materials studied, with a half-wave potential ($E_{1/2}$) of 0.977 V vs RHE and a mass activity of 0.86 mA/ μ g_{Pd} in 1 M KOH, both values being superior to those of commercial Pd/C electrocatalysts. Moreover, it maintained robust durability after 20,000 potential cycles with a minimal degradation in $E_{1/2}$ of 10 mV. The enhanced performance and stability are ascribed to the uniform elemental distribution of Pd and Co and the Co-containing N-doped carbon (Co–N–C) structures. In anion exchange membrane fuel cell (AEMFC) tests, the peak power density of the cell employing a BMOF-derived Pd₃Co cathode reached 1.1 W/cm² at an ultralow Pd loading of 0.04 mg_{Pd}/cm². Strategies developed herein provide promising insights into the rational design and synthesis of highly active and durable ORR electrocatalysts for alkaline fuel cells.

KEYWORDS: anion exchange membrane fuel cells, oxygen reduction reaction, Pd—Co electrocatalysts, metal-organic frameworks, Co–N–C

1. INTRODUCTION

With the continued consumption of fossil fuels and increasing energy demands, the development of sustainable energy technologies to mitigate CO2 emissions has drawn increasing worldwide attention. 1,2 Fuel cells (FCs) represent a promising technology with tremendous potential for large-scale applications due to their high-efficiency energy conversion.^{3–5} Proton exchange membrane fuel cells (PEMFCs) represent an effective approach for powering electric vehicles. However, PEMFCs require significant amounts of expensive Pt-based (and related precious-metal-based) catalysts to accelerate the sluggish oxygen reduction reaction (ORR) at the cathode, which is one of the key challenges for the commercialization of fuel cell technologies. 6-10 These constraints have precluded the broad application of PEMFCs. As an alternative, anion exchange membrane fuel cells (AEMFCs), which operate at high pH, have attracted significant interest because they enable the use of non-precious-metal-based catalysts. 11-13 To facilitate the ORR kinetics in alkaline media, a variety of investigations have focused on the development of cost-effective electrocatalysts with high performance and robust long-term durability, including precious-metal-based alloys, 14–17 transition metals and metal oxides, 18–20 metal nitrides, 21–24 perovskites, 22,25 and metal-containing nitrogen-doped carbon (M–N–C).

Recently, metal-organic framework (MOF)-derived catalysts have emerged as a promising family of ORR electrocatalysts. MOF-derived carbon materials generally exhibit a highly porous structure, which is beneficial for mass

Received: June 6, 2022 Accepted: September 13, 2022



transport.30,33 In addition, nitrogen species derived from Ncontaining ligands in MOFs are able to anchor metallic nanoparticles or single metal atoms to the carbon support, which is believed to accelerate the ORR kinetics and enhance the stability of the catalysts. 34,35 Lou and co-workers developed a Co-N-C material from zeolitic imidazolate frameworks (ZIFs), which showed promising activity toward the ORR and oxygen evolution reactions (OERs).³⁶ Li and co-workers prepared isolated Fe atoms on N-doped carbons from ZIF-8, which exhibited excellent ORR activity in both alkaline and acidic media.³⁷ We previously reported on Pt-Co alloys prepared from bimetallic MOFs (BMOFs), derived from a mixture of ZIF-8 and ZIF-67. Both the ordered PtCo and the disordered PtCo2 exhibited high activity and robust stability, which were ascribed to the synergistic interactions between Pt-Co nanoparticles and the single-atom Co-N-C structures.38

Herein, we report on a group of low-palladium-loading (\sim 10 wt %) Pd_xCo (x = 1-6) bimetallic nanoparticles embedded in a Zn-Co BMOF-derived highly porous carbon support. Under high-temperature treatment, the Zn centers evaporate and create a large number of cavities, which increase porosity and benefit mass transport. At the same time, Co catalyzes the formation of N-doped carbon nanotubes, which can increase the conductivity of the carbon support and wrap the metal nanoparticles to further improve stability. The structure and composition of the electrocatalysts were comprehensively characterized by X-ray diffraction (XRD), X-ray photoelectron spectroscopy (XPS), inductively coupled plasma optical emission spectroscopy (ICP-OES), scanning transmission electron microscopy (STEM) imaging, and energy-dispersive spectroscopy (EDX). After optimizing the annealing temperature and electrocatalyst composition, the BMOF-derived Pd₃Co catalysts were identified as having the highest activity and stability toward the ORR. In membrane electrode assembly (MEA) tests, the material reached an impressive peak power density in MEA of >1 W/cm² at an ultralow Pd loading of 0.04 mg_{Pd}/cm².

2. EXPERIMENTAL SECTION

2.1. Materials. Zinc nitrate $(Zn(NO_3)_2 \cdot 6H_2O)$, cobalt nitrate $(Co(NO_3)_2 \cdot 6H_2O)$, 2-methylimidazole, 1-methylimidazole, palladium(II) nitrate dihydrate $(Pd(NO_3)_2 \cdot 6H_2O)$, ethanol, methanol, and Nafion (5 wt %) were purchased from Sigma-Aldrich. Carbon-supported Pd/C (20 wt %) and Pt/C (20 wt %) were purchased from Johnson Matthey. All chemicals were used as received without further purification.

2.2. Synthesis of BMOF Zn_xCo_v-Derived Carbon Materials. ZIF-67 and ZIF-8 were used as the carbon precursors (ZIF: zeolitic imidazolate frameworks). ZIF-67 is composed of a cobalt center coordinated by four imidazolate groups, while ZIF-8 has zinc as the metal center. The synthesis method was as reported previously.³⁸ Typically, a mixture of $Co(NO_3)_2 \cdot 6H_2O$ and $Zn(NO_3)_2 \cdot 6H_2O$ with different molar ratios of Co^{2+}/Zn^{2+} was dissolved in a mixed solvent of 40 mL ethanol and 40 mL methanol, where the total molar amounts of Zn²⁺ and Co²⁺ were 6 mmol, with stoichiometric numbers represented by x and y in moles. Another mixture of 2methylimidazole (1.97 g) and 1-methylimidazole (0.49 g) with 40 mL methanol and 40 mL ethanol was then added under magnetic stirring. The solution was left standing still for 48 h at room temperature. The formed precipitate was collected by centrifugation, washed with methanol, and dried in an oven at 60 °C. The assynthesized BMOF-Zn_xCo_y particles were transferred into a flow furnace and heated to 300 °C for 1.5 h and then to 800 °C for 2 h in a flowing forming gas (5% H_2 + 95% N_2). Pyrolyzed BMOF- Zn_xCo_y materials were collected after the furnace was turned off and cooled down.

2.3. Synthesis of BMOF-Derived Pd_xCo_y **Materials.** BMOF-derived Pd_xCo_y materials were prepared by the impregnation method. In a typical synthesis of the Pd₃Co material derived from pyrolyzed BMOF-Zn₁₅Co, 50 mg of pyrolyzed BMOF-Zn₁₅Co was suspended in 1.135 mL of 0.05 M Pd(NO₃)₂ solution. After ultrasonication for 30 min, the mixture was heated to 80 °C with magnetic stirring to evaporate extra moisture to form a smooth slurry, which was kept overnight and then dried in an oven at 60 °C. The formed black powder was transferred into a flow furnace and annealed under a flowing forming gas (5% H₂ + 95% N₂). The temperature of the furnace was initially set at 300 °C for 2 h and further ramped up to 400 °C for an additional 2 h of annealing. Pd₃Co was collected after the furnace was turned off and cooled down.

2.4. Structural Characterization. The crystal structures of all of the synthesized BMOFs, pyrolyzed BMOFs, and BMOF-derived Pd_rCo_v materials were confirmed by powder X-ray diffraction (XRD) using a Rigaku Ultima VI Diffractometer, measured from 15 to 90° at a scan rate of 4° min⁻¹. Both the metal loading and the ratio of Pd/Co in the Pd, Co, catalysts were measured by inductively coupled plasma optical emission spectroscopy (ICP-OES, SPECTRO ARCOS FHE12). X-ray photoelectron spectroscopy (XPS) spectra were collected with a Surface Science Instruments SSX-100 operated under a working pressure at 2×10^{-9} Torr. Scanning transmission electron microscopy (STEM) images and energy-dispersive X-ray (EDX) maps were taken on a Thermo Fisher Scientific Spectra 300 STEM electron microscope with a Bruker Dual X detector at 300 kV and an FEI Tecnai F-20 with an Oxford X-Max detector at 200 kV. The Pd_xCo ethanol dispersions were drop-casted on lacey carbon on Cu TEM grids and ambient-dried. EDX maps were denoised with principal component analysis. Electron energy loss spectroscopy (EELS) spectra and STEM images of single Co atoms were taken on a fifth-order aberration-corrected STEM (Cornell Nion UltraSTEM 100) operated at 100 keV.

2.5. Electrochemical Characterization. Electrochemical measurements were performed in 1.0 M KOH on a Pine Instruments WaveDriver 200 Bipotentiostat. In all electrochemical measurements, 5 mg of the BMOF-derived Pd, Co, catalyst was mixed with 0.5 mL of a 0.25 wt % Nafion/ethanol solution and subsequently sonicated for approximately 30 min to form homogeneous catalyst inks. Five microliters of the resulting catalyst ink were loaded onto a 5 mm diameter glassy carbon (GC) electrode, followed by thermal evaporation of the solvent under an infrared lamp. The resulting BMOF-derived Pd_xCo_y catalyst loadings are listed in Table S1. Similarly, 5 mg of 20 wt % Pd/C catalyst was mixed with 1.0 mL of 0.25 wt % Nafion/ethanol solution and 5 μL of ink was transferred onto a GC electrode to achieve a loading of 25.5 μ g cm⁻², a common value for comparison in fuel cell tests. A Ag/AgCl in 1.0 M KCl solution served as the reference electrode, and a large surface area graphite rod was used as the counter electrode. ORR measurements were carried out with a rotating disk electrode (RDE, Pine Instruments) in an oxygen-saturated 1.0 M KOH solution at room temperature. ORR polarization profiles were obtained at 5 mV/s and 1600 rpm. The background capacitive current measured in Arsaturated 1.0 M KOH solution was subtracted to process and plot the ORR profiles. Cyclic voltammetric profiles were obtained at 50 mV/s in Ar-saturated 1.0 M KOH. Durability tests were carried out by continuously cycling the potential from 0.6 to 1.0 V at 100 mV/s for 20,000 cycles in O₂-saturated 1 M KOH. The ORR profiles after 20,000 cycles were measured in a fresh 1.0 M KOH electrolyte to avoid potential contamination from dissolved metal species in the solution. RRDE measurements were carried out with a rotating ringdisk electrode (RRDE, Pine Instruments) to detect the H₂O₂ generated at the disk during the oxygen reduction reaction. The RRDE with a GC disk (0.2475 cm²) and a Pt ring (0.1866 cm²) was calibrated to have a collection efficiency of 37% using 10 mM K₃Fe(CN)₆ with a 0.1 M K₂SO₄ supporting electrolyte. RRDE measurements were performed in 1.0 M KOH at 5 mV/s and 1600

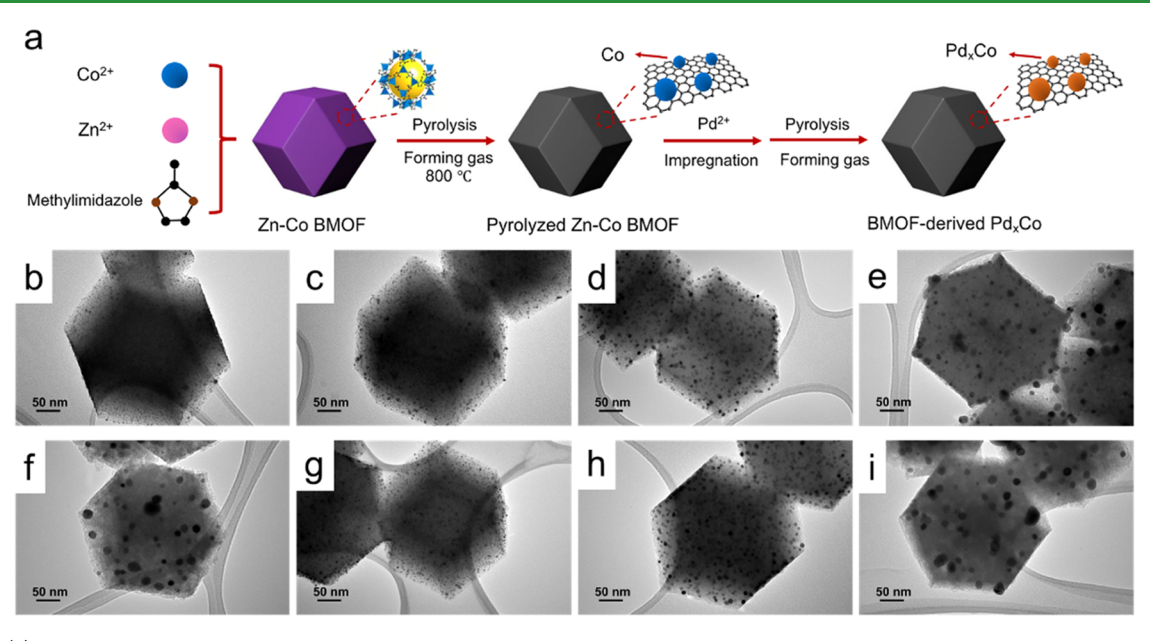


Figure 1. (a) Schematic synthesis procedure of BMOF-derived Pd_xCo. TEM images of pyrolyzed BMOF-Zn₂₀Co-derived Pd₂Co materials annealed at (b) 200–300 °C, (c) 200–400 °C, (d) 200–500 °C, (e) 200–600 °C, (f) 200–700 °C, (g) 300–400 °C, (h) 300–500 °C, and (i) 300–600 °C.

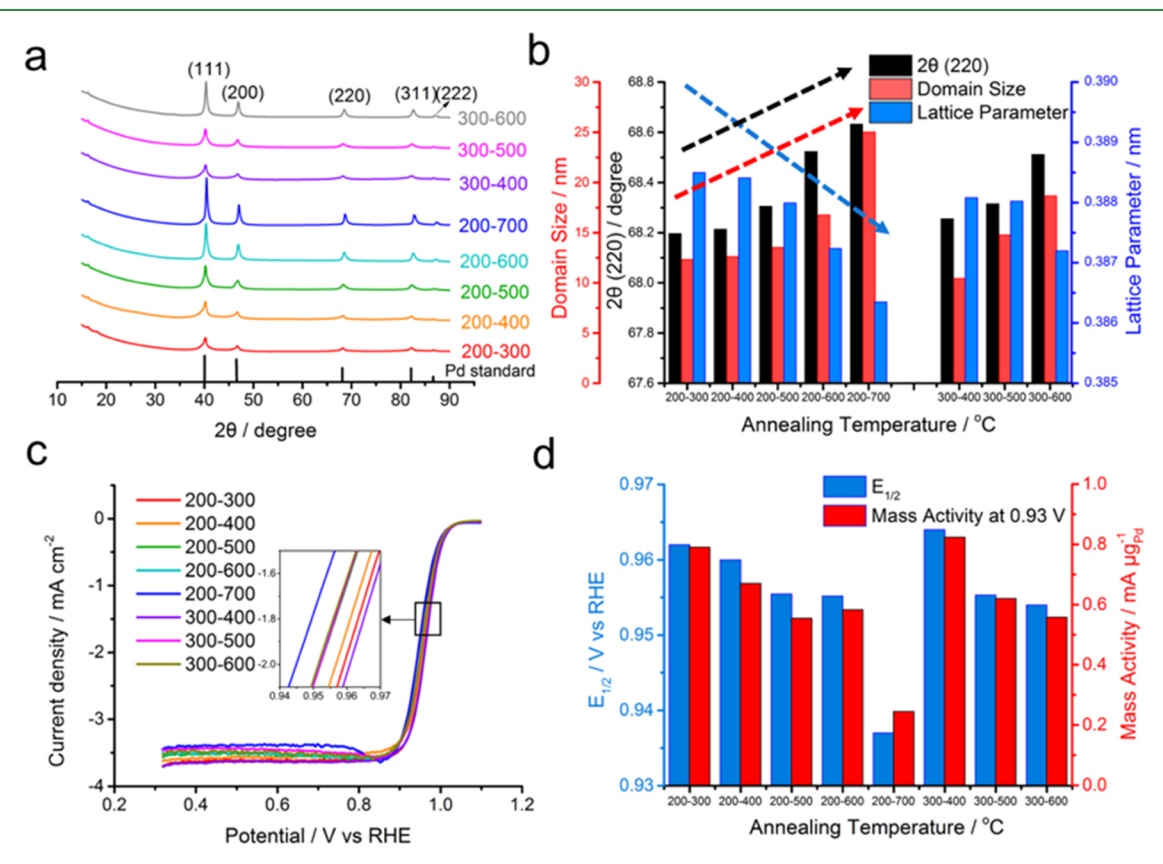


Figure 2. (a) XRD patterns of BMOF-Zn₂₀Co-derived Pd₂Co materials annealed at different temperatures. The black vertical lines correspond to standard Pd (ICSD #64920). (b) Analysis of $2\theta(220)$ angles, domain sizes, and lattice parameters. (c) ORR polarization curves of BMOF-Zn₂₀Co-derived Pd₂Co in O₂-saturated 1.0 M KOH at a scan rate of 5 mV/s and a rotation rate of 1600 rpm. Catalyst loading: 19.7 μ g_{Pd}/cm². (d) Comparison of the ORR mass activity at 0.93 V vs RHE and half-wave potentials ($E_{1/2}$).

rpm, and the ring potential was held at 1.3 V vs RHE to be sufficiently high to oxidize any H_2O_2 generated at the disk.

2.6. Fuel Cell Tests. The H_2 – O_2 fuel cells were tested (850 and 850e Multi Range, Scribner Associates Co.) under galvanic mode using humidified (100% RH) H_2 and O_2 gases (Airgas, UHP 300).

The cell temperature was set to 80 $^{\circ}$ C, and the flow rate of both H_2 and O_2 gases was 500 mL/min with 0.2 MPa of backpressure. The catalyst powder was dispersed in a poly(p-terphenyl-piperidinium) (QAPPT) ionomer solution with a ratio of 4:1 (catalyst/ionomer) and then sprayed onto each side of the QAPPT membrane. The areas

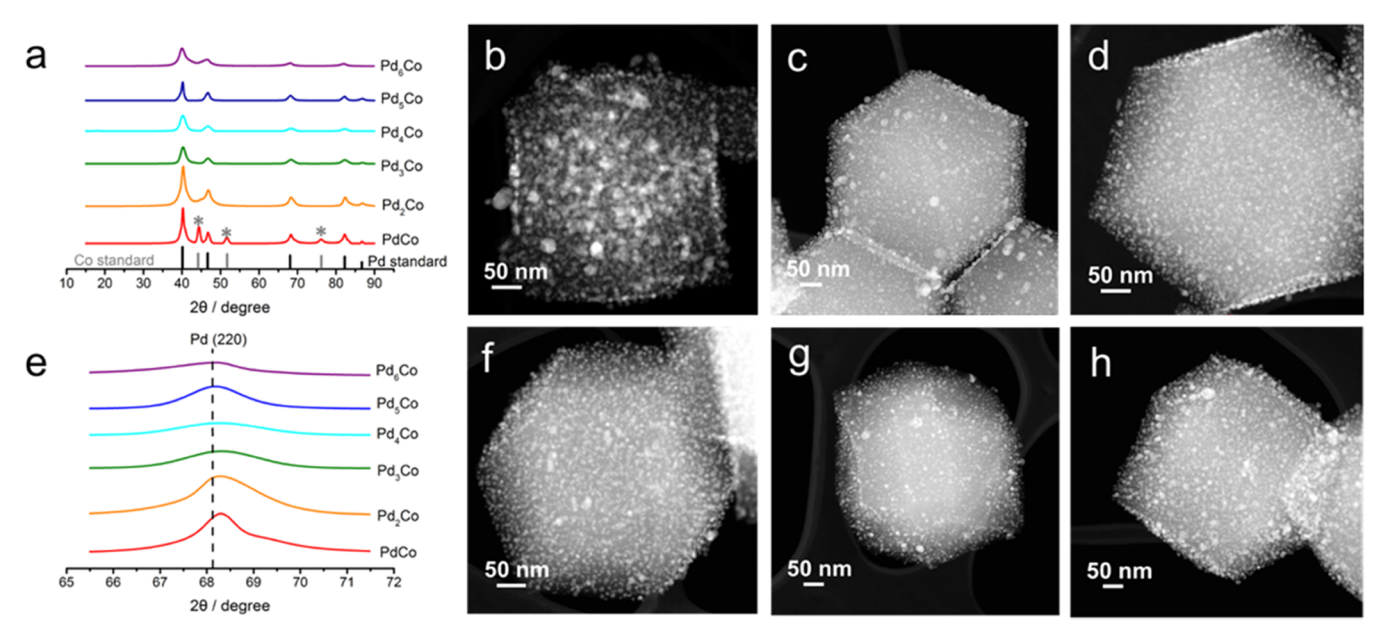


Figure 3. (a) XRD patterns of Pd_xCo (x = 1-6). The black and gray vertical lines correspond to standard Pd (ICSD #64920) and Co (ICSD#44989), respectively. (e) Expanded (220) diffraction peaks in the region of 65–72°. HAADF-STEM images of BMOF-derived (b) PdCo, (c) Pd₂Co, (d) Pd₃Co, (f) Pd₄Co, (g) Pd₅Co, and (h) Pd₆Co.

of electrodes were 4 cm². The catalyst loadings for commercial PtRu/C (Fuel Cell Store) on the anode were 0.4 $\rm mg_{PtRu}/\rm cm^2$, and the loading of BMOF-derived Pd₃Co on the cathode was varied to find the optimal value. Gas diffusion layers were two pieces of carbon paper (AvCard GDS3250). Electrochemical impedance spectroscopy (EIS) was measured at 0.2 A/cm² with an AC RMS amplitude of 5% of the corresponding current. The measurement was conducted over the frequency range of 0.1 Hz to 10 kHz.

3. RESULTS AND DISCUSSION

3.1. Optimization of Annealing Temperature. 3.1.1. Synthesis and Structural Characterization. The BMOF-derived Pd_x Co catalysts were prepared via a facile method (details in the Experimental Section). 34,38 As shown in Figure 1a, Zn-Co BMOFs were synthesized with Co²⁺ and Zn²⁺ as metal centers and methylimidazole groups as organic linkers. Zn centers in the Zn-Co BMOF precursors evaporated during the first pyrolysis process at 800 °C, forming the pyrolyzed Zn-Co BMOFs with Co metal particles on the MOF-derived nitrogen-doped carbon support. The Pd precursor $(Pd(NO_3)_2)$ was then added to the pyrolyzed Zn-Co BMOFs by an impregnation method. In the subsequent high-temperature treatment, Pd2+ was reduced to Pd0 under the reducing atmosphere of forming gas (5% H₂ and 95% N₂) and alloyed with Co to form Pd_xCo metal particles. To find an optimal annealing condition, BMOF-Zn₂₀Co-derived Pd₂Co materials were treated at different temperatures: 200-300, 200-400, 200-500, 200-600, 200-700, 300-400, 300-500, and 300-600 °C.

The resulting materials were characterized via transmission electron microscopy (TEM), as shown in Figure 1b–i, indicating a uniform distribution of metal nanoparticles on the BMOF-derived polyhedral carbon structures. The size of the metal nanoparticles increased at higher annealing temperatures suggesting coalescence. For the samples in which the annealing temperature was above 500 $^{\circ}$ C, larger metal nanoparticles (>20 nm) appeared, likely due to particle aggregation. The XRD patterns of Pd₂Co, annealed at different

temperatures, are shown in Figure 2a with expanded XRD regions in Figure S1. The diffraction peaks near 40, 46, 68, 82, and 86° were ascribed to the (111), (200), (220), (311), and (222) planes in a typical single-phase face-centered cubic (fcc) lattice structure. Compared to the Pd fcc standard (ICSD#64920), the peak positions of Pd₂Co shifted to higher angles with increasing annealing temperature due to a lattice contraction from the incorporation of the smaller Co atoms into the Pd lattice. The change in 2θ (for the 220 reflection), domain size, and lattice parameter, calculated via Bragg's law and the Debye-Scherrer equation, is summarized in Figure 2b. With increasing annealing temperature, the domain size increased due to particle aggregation, which is consistent with the TEM images. The lattice parameter decreased, indicating a larger lattice contraction upon high-temperature treatment of the Pd-Co alloys.

3.1.2. Electrochemical Analysis. In an effort to identify the optimal annealing temperature, we used the BMOF- Zn_{20} Coderived Pd_2 Co catalysts as a test case. Figure S2 presents the cyclic voltammograms (CVs) obtained at 50 mV/s in an Arsaturated 1.0 M KOH solution of the BMOF-derived Pd_2 Co catalysts treated at different annealing temperatures. The relatively wide double layer of BMOF-derived catalysts was attributed to the high surface area of the BMOF-derived carbons. The width of the double layer decreased with increasing annealing temperature, suggesting a decrease in the surface area due to the formation of large cavities in the carbon structure, as clearly observed in the TEM images in Figure $1f_1$ i.

The oxygen reduction reaction (ORR) polarization curves obtained in an O₂-saturated 1.0 M KOH, at a scan rate of 5 mV/s and a rotation rate of 1600 rpm, are shown in Figure 2c. The inset in Figure 2c presents an expanded view of the half-wave potential ($E_{1/2}$) region. Among the Pd₂Co catalysts studied, the one annealed at 300–400 °C exhibited the highest $E_{1/2}$ value of 0.964 V vs RHE. The mass activities at 0.93 V and the half-wave potentials are summarized in Figure 2d. As for the mass activity, Pd₂Co annealed at 300–400 °C achieved the highest activity of 0.82 mA/ μ gp_d. As a result, 300–400 °C

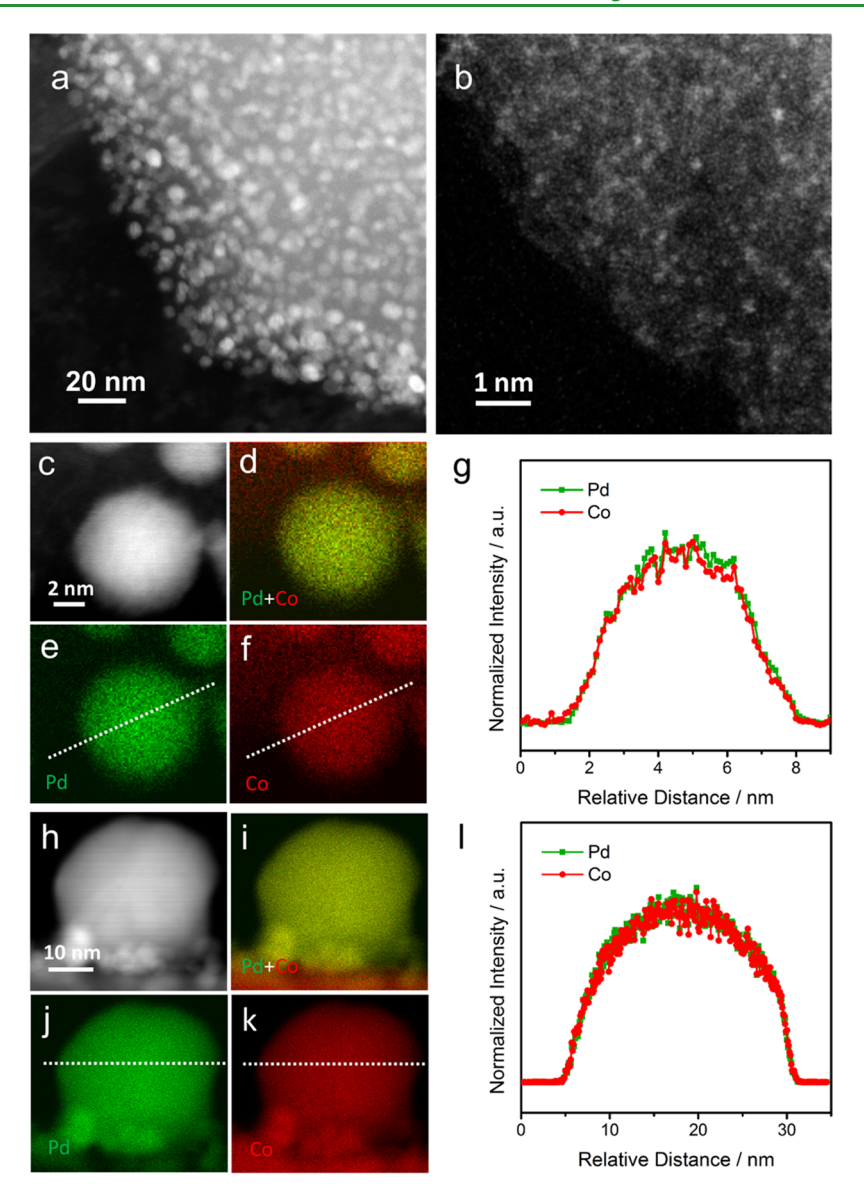


Figure 4. (a) STEM image of BMOF-derived Pd_3Co . (b) High-magnification STEM image of Co single atoms on the MOF-derived carbon structures. (c) High-magnification STEM image of BMOF-derived Pd_3Co . EDX elemental maps of (e) Pd (green) and (f) Pd (red) and (d) their composite map. (g) Normalized EDX elemental line profiles of Pd and Pd Co along with the white dashed lines in the EDX maps (e) and (f), respectively. (h) High-magnification STEM image of BMOF-derived Pd_3Co after 20,000 cycles. EDX elemental maps of (j) Pd (green) and (k) Pd (red) and (i) their composite map. (l) Normalized EDX elemental line profiles of Pd and Pd Co along with the white dashed lines in the EDX maps (j) and (k), respectively.

represents the optimized annealing temperature for the BMOF-derived Pd_2Co catalysts.

To validate this observation, different temperature treatments were applied to BMOF-derived Pd_4Co and Pd_6Co . Their TEM images and XRD patterns are shown in Figures S3–S7, which exhibit similar trends to those of the BMOF-derived Pd_2Co . For both the BMOF-derived Pd_4Co and Pd_6Co , samples annealed at 300–400 °C exhibited the highest mass activity at 0.93 V vs RHE (Figures S8 and S9), confirming that the optimized annealing temperature is 300–400 °C.

3.2. Optimization of Electrocatalyst Composition (Nominal Atomic Ratio of Pd/Co). *3.2.1.* Structural Characterization. Having identified the optimal annealing temperature, the composition of the BMOF-derived Pd—Co nanoparticles was subsequently optimized. To achieve a 10 wt % Pd loading in BMOF-derived Pd—Co samples, PdCo,

Pd₂Co, Pd₃Co, Pd₄Co, Pd₅Co, and Pd₆Co were prepared from BMOF- Zn_xCo_y precursors with different Zn/Co(x/y) ratios. The tabulated x/y values, Co wt %, Pd wt %, and ratios of Pd/ Co, obtained from inductively coupled plasma optical emission spectroscopy (ICP-OES) measurements, are presented in Table S1. As shown in Figure 3a, the XRD patterns of BMOF-derived Pd_xCo (x = 1-6) with different Pd/Conominal atomic ratios, after high-temperature treatment at 300-400 °C, are consistent with a typical fcc lattice structure. At a Pd/Co atomic ratio of 1:1, the small diffraction peaks near 44, 52, and 76°, labeled with asterisks, were ascribed to the (111), (200), and (220) planes from the fcc metallic Co structure, consistent with the standard XRD pattern of metallic Co (ICSD#44989). These metallic Co diffraction peaks were due to the relatively high Co content of 6.79 wt % in the BMOF-Zn₄Co precursors. The 2θ (220) diffraction peaks in an expanded view exhibited a slight shift to higher angles

ACS Applied Materials & Interfaces

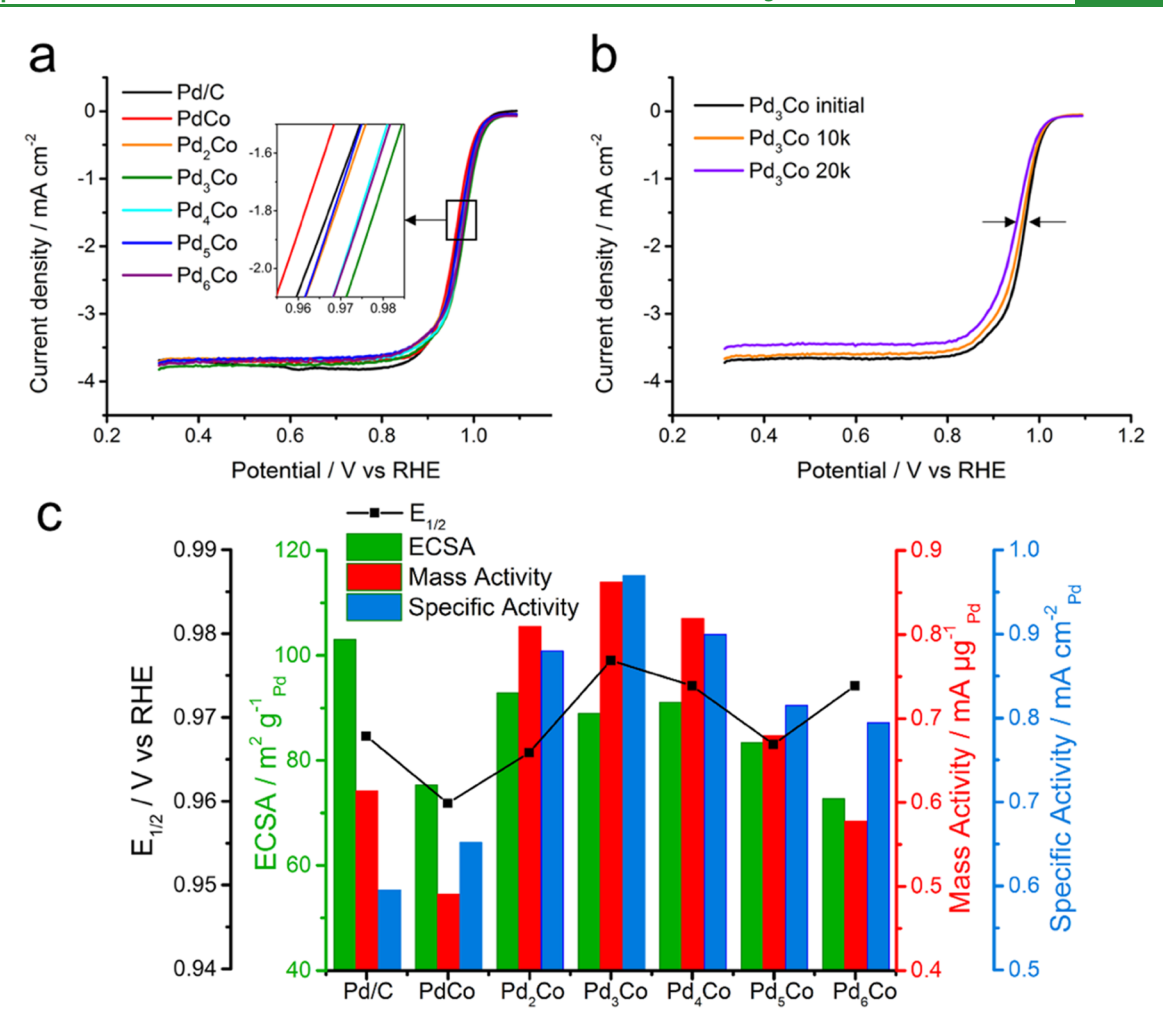


Figure 5. (a) ORR polarization curves of BMOF-derived Pd_xCo (x = 1-6) in O_2 -saturated 1.0 M KOH at a scan rate of 5 mV/s and a rotation rate of 1600 rpm. (b) ORR polarization curves of BMOF-derived Pd_3Co in O_2 -saturated 1.0 M KOH at 1600 rpm and 5 mV/s after 10 and 20 k potential cycles from 0.6 to 1.0 V at 100 mV/s. (c) Comparison of the ECSA (in green), mass activity (in red) at 0.93 V vs RHE, specific activity (in blue) at 0.93 V vs RHE, and half-wave potential ($E_{1/2}$).

compared to the Pd standard pattern (Figure 3e), which is consistent with a lattice contraction caused by the smaller atomic radius of the incorporated Co atoms. The peak position shifted to higher angles with decreasing x value in Pd_x Co (i.e., higher Co relative content), indicating the incorporation of more Co atoms into the Pd lattice.

The morphologies of BMOF-derived Pd_xCo (x = 1-6) were examined by high-angle annular dark-field (HAADF) scanning transmission electron microscopy (STEM) imaging (Figure 3b-d, f-h). The Pd-Co alloy particles are significantly brighter than the MOF-derived carbon support since the HAADF image intensity is proportional to the atomic number $(I \propto Z^{1.7})$. Pd-Co nanoparticles were uniformly distributed on the MOF-derived polyhedron carbon supports. The particle size distribution (PSD) histograms, based on more than 300 particles, are shown in Figure S11. At a Pd/Co atomic ratio of 1:1, there were some metal nanoparticles larger than 30 nm, which may be due to the higher total metal loading relative to other compositions. Similarly, large particle sizes were also observed in PtCo alloys in our previous work.³⁸ Pd₃Co and Pd₄Co showed relatively smaller particle sizes of 5.4 ± 1.5 nm (average \pm standard deviation, S_d) and 5.0 \pm 1.2 nm, respectively. Figure 4c,d presents energy-dispersive X-ray spectroscopy (EDX) maps of Pd (green) and Co (red) from

a 6.5 nm sized Pd₃Co nanoparticle. The EDX maps are denoised via principal component analysis decomposition. The EDX composition maps of Pd and Co (Figure 4e,f) suggested a relatively homogeneous elemental distribution of Pd and Co. The normalized EDX line profiles (Figure 4g) along the dashed lines in Figure 4e,f confirmed the uniform distribution of Pd and Co across the metal alloy nanoparticles. This provides compelling evidence of the formation of a uniform Pd-Co alloy at the near-atomic scale, which is consistent with the observation of single-phase Pd₃Co alloys from the XRD patterns in Figure 3a. Besides the EDX elemental distribution, the Pd/Co atomic ratio in Pd₃Co was calculated from quantitative EDX analysis based on the Cliff-Lorimer equation. 40 Relative atomic contents of Pd and Co were calculated to be 74.21 and 25.8% from the Pd Llpha edge at 2.8 keV and the Co K α edge at 6.9 keV, respectively (Figure S12a). The calculated atomic ratio of Pd/Co was 2.9, which is consistent with the intended stoichiometry of Pd₃Co and the ICP results (Table S1). The combination of microscopic-level STEM-EDX mapping with the quantitative EDX analysis unambiguously indicates that the BMOF-derived Pd₃Co nanoparticles have a homogeneous elemental distribution of Pd and Co with the intended Pd/Co ratio of 3:1.

Research Article

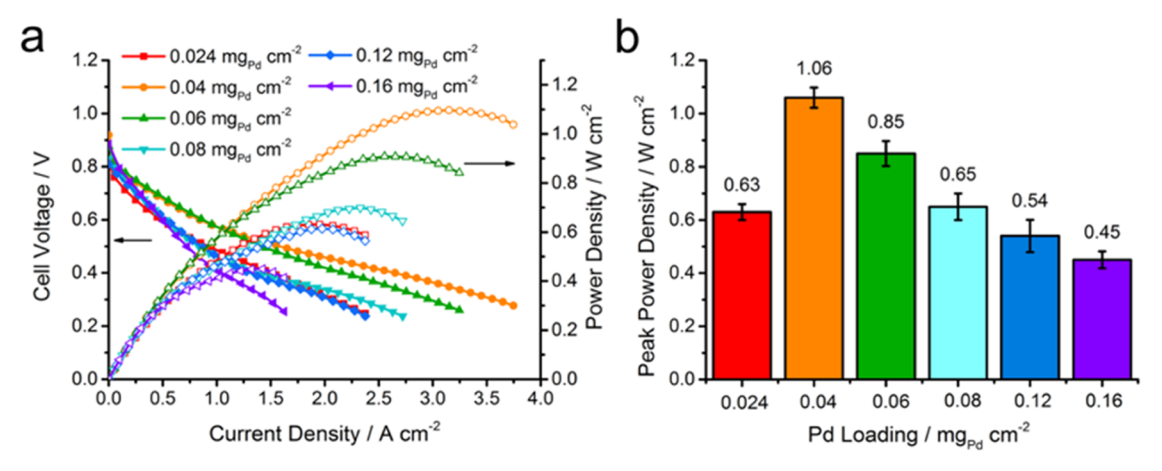


Figure 6. (a) Alkaline exchange membrane fuel cell (AEMFC) tests with H_2 and O_2 at 80° C and 100% RH. Anode catalyst: 60 wt % Pt-Ru/C (Johnson Matthey, 0.4 mg_{PtRu} cm⁻²). Cathode catalyst: BMOF-derived Pd₃Co with different loadings. (b) Peak power density comparison of BMOF-derived Pd₃Co cathode with different loadings.

The carbon support in the BMOF-derived Pd₃Co materials was also investigated at the atomic scale with STEM. In Figure 4b, around 3 Å sized bright spots, dispersed on the carbon support, suggest the presence of atomically dispersed Co atoms, according to electron energy loss spectroscopy (EELS) analysis (Figure S12b). After the high-temperature annealing treatment, the imidazole ligands from the BMOF precursors contribute to the high-level doping of nitrogen. X-ray photoelectron spectra (XPS) (Figure S13) suggested the presence of N and the interaction between N and Co by the subpeak at 399.5 eV in the N 1s XPS spectra, which was ascribed to a Co- N_x structure (Figure S13c). STEM and XPS spectroscopic analyses evidenced the existence of Cocontaining N-doped carbons (Co-N-C), which have been widely reported as active sites in MOF-derived catalysts to bind oxygen and promote the ORR kinetics. 29,41-43

3.2.2. Electrochemical Analysis. The electrochemical activities of BMOF-derived Pd_x Co (x = 1-6) catalysts toward the ORR were investigated in alkaline electrolyte using rotating disk electrode (RDE) voltammetry. The Pd loadings are summarized in Table S1. The polarization curves were obtained in an O₂-saturated 1.0 M KOH electrolyte at a scan rate of 5 mV/s and 1600 rpm, as shown in Figure 5a. The $E_{1/2}$ of the BMOF-derived Pd₃Co was 0.977 V vs RHE, which is 10 mV more positive than that of commercial 20 wt % Pd/C and 57 mV more positive than that of commercial 20 wt % Pt/ C (Figure S14). As shown in Figure S15, the Tafel slope values of BMOF-derived Pd_x Co (x = 1-6) electrocatalysts are comparable to that of Pd/C catalysts (43 mV/dec) but are significantly lower than that of Pt/C catalysts (56 mV/dec), indicating enhanced ORR kinetics of BMOF-derived Pd_xCo (x = 1-6) when compared to Pt/C catalysts. The $E_{1/2}$ values, electrochemical surface areas (ECSAs), mass activities at 0.93 V, and specific activities at 0.93 V are summarized in Figure 5c. The BMOF-derived Pd₃Co exhibited the highest mass activity and specific activity with values of 0.86 mA/ μ g_{Pd} and 0.97 mA cm_{Pd}⁻², respectively, which are nearly 1.4 times and 1.6 times higher than those of commercial Pd/C (0.613 mA/ μ g_{Pd} and 0.595 mA cm_{Pd}⁻², respectively). In addition, as shown in Figure S16, BMOF-derived Co-N-C also exhibited promising ORR activity with an $E_{1/2}$ of 0.932 V vs RHE, which is 12 mV more positive than that of commercial Pt/C. Therefore, the catalytic enhancement of the BMOF-derived Pd₃Co

toward ORR is ascribed to the active sites in the Pd–Co alloys as well as the contribution from single-atom Co-N-C structures.³⁸

The ORR selectivity of the BMOF-derived Pd_3Co was assessed using rotating ring-disk electrode (RRDE) voltammetry to measure the peroxide yield and the electron-transfer number (n). As shown in Figure S17, the ring current obtained from BMOF-derived Pd_3Co was below 14 μ A. The peroxide yield was less than 8%, and the calculated n value was above 3.85 over the potential region between 0.3 and 0.9 V, both of which are comparable to a commercial Pd/C catalyst.

The stability of the BMOF-derived Pd₃Co was evaluated in an O2-saturated 1.0 M KOH electrolyte by scanning the potential at a rate of 100 mV/s over the potential range of 0.6-1.0 V vs RHE, following an accelerated stress test (AST) protocol recommended by the U.S. Department of Energy. The CV and ORR polarization profiles at 1600 rpm after 10,000 and 20,000 cycles are compared with the initial ones in Figures S18 and 5a, respectively. After 10,000 and 20,000 cycles, the hydrogen region at ~0.1 V decreased when compared to the initial CV profile, indicating a decrease of the ECSA. After 10,000 cycles, the $E_{1/2}$ shifted in the negative direction by less than 5 mV, indicating excellent activity retention. After 20,000 cycles, the $E_{1/2}$ shifted negatively by 10 mV, a value of the $E_{1/2}$ that is still comparable to that of a commercial Pd/C catalyst. The shift in the $E_{1/2}$ could be due, at least, in part, to the decrease in the ECSA. HAADF-STEM images and PSD histograms of BMOF-derived Pd₃Co after 10,000 and 20,000 cycles are presented in Figure S19. After cycling, most of the small Pd-Co alloy particles were still embedded in the carbon support with the emergence of a few aggregated larger particles. EDX maps of Pd₃Co after 20,000 cycles are shown in Figure S20, where some larger metal particles are evident. Figure 4h-k presents an STEM image and EDX maps of a single large metal particle of 25 nm in size. The EDX composition maps of Pd and Co (Figure 4j,k) indicated that Pd and Co were still homogeneously distributed throughout the particle after 20,000 cycles. The normalized EDX line profiles (Figure 41) along the dashed lines in Figure 4j,k suggest a uniform distribution of Pd and Co across the metal alloy nanoparticles. The intimate anchoring of metal particles on the MOF-derived carbon support and uniform elemental distribution of Pd and Co in the metal particles

contributed to the stability of the BMOF-derived Pd-Co catalysts.

3.3. Fuel Cell Tests. The electrocatalytic performance of optimized BMOF-derived Pd₃Co was further assessed under realistic membrane electrode assembly (MEA) conditions. The BMOF-derived Pd₃Co, at different loadings (details in Table S2), was used as the cathode catalyst, while a commercial 60 wt % PtRu/C was used as the anode catalyst at a loading of 0.4 mg_{PtRu}/cm². The resulting polarization curves are shown in Figure 6a. A Pd loading of 0.04 mg_{Pd}/cm², on the cathode side, showed the highest peak power density of 1.1 W/cm² at 3.2 A/ cm². It should be noted that the Pd loading employed here is ultralow, representing only 10% of the typical precious-metal loading of 0.4 mg/cm². The averaged peak power densities with error bars are summarized in Figure 6b. With increasing amounts of BMOF-derived Pd₃Co in the cathode, the value of the peak power density initially increased, ostensibly due to the addition of active sites. It subsequently decreased likely due to mass transport limitations from the increasing thickness of the catalyst layer. The electrochemical impedance spectroscopy (EIS) profiles at 200 mA/cm² over the frequency range of 0.1 Hz to 10 kHz are shown in Figure S21a. The EIS data were fitted based on the equivalent circuit shown in Figure S21b, and the fitting parameters are listed in Table S3. With an increase in the catalyst loading from 0.024 to 0.16 mg_{Pd}/cm², the ohmic resistances of MEAs $(R_{\rm ohm})$ increased from \sim 0.02 to \sim 0.05 Ω , which is ascribed to the additional resistance from the thicker catalyst layer. On the other hand, the chargetransfer resistance $(R_1 + R_2)$ decreased from ~0.09 to ~0.05 Ω because more active sites can facilitate charge-transfer kinetics at higher catalyst loading.

The durability of BMOF-derived Pd₃Co in AEMFCs was preliminarily evaluated at 50 mA/cm² (Figure S22a), which showed a lifetime of around 100 h. At the beginning of the test, a relatively rapid drop in voltage was observed, suggesting the quick water flooding of the anode. 45 After a voltage dip at around 9 h, the cell voltage decreased at a slower rate in the subsequent 10-90 h. The voltage dips are likely related to the water droplets formed in the gas diffusion layer. 46,47 When the formed water droplets are expelled from the system by the flowing gases, the cell voltage can recover to some extent. Similar phenomena were observed at a higher current density of 200 mA/cm² (Figure S22b). To explore the reasons for the degradation in AEMFCs, the EIS profiles, before and after 24 h test at 200 mA/cm², were collected and are shown in Figure S23a. After the 24 h MEA test, the low-frequency resistance increased significantly, indicating a larger mass transport resistance compared to the initial state. To further deconvolve the kinetic information contained in the EIS profiles, the distribution of relaxation times (DRT) method⁴⁸ was applied to extract the characteristic times from the EIS data. As shown in Figure S23b, the peaks in the DRT profiles can be assigned to the processes of the hydrogen oxidation reaction (HOR), ORR, and anode/cathode mass transport. 45,49 Before the MEA test, it only showed three resistance peaks related to the HOR (P1 and P2) and ORR (P3). After 24 h of testing, the increase of P1 and P2 suggested slower charge-transfer kinetics for the HOR, while a smaller increase in the peak for the ORR (P3) was observed. Moreover, peaks related to mass transport resistance (P4 and P5) became evident after MEA testing, especially for the anode, which was likely caused by water flooding. In addition, BMOF-derived Pd₃Co was tested for 24 h on an RDE at 0.7 V vs RHE (region of ORR diffusionlimited current) to simulate a constant voltage operation. The CV and ORR profiles, STEM images, and PSD histograms, compared with the initial state, are presented in Figure S24. After 24 h, the $E_{1/2}$ exhibited a slight negative shift of 3 mV. The Pd-Co alloy particles were embedded in the carbon support with an even distribution, and the particle size distribution was almost the same as in the initial state, which indicated that the BMOF-derived Pd₃Co catalyst remained stable at 0.7 V vs RHE for 24 h. Therefore, in this case, the degradation in AEMFC performance was not mainly due to the cathode catalyst degradation but rather related to the mass transport and water management issues, which are key challenges for enhancing the performance and long-term durability of AEMFCs. S0,51 The optimization of water management, the stability of membrane, and the improvement of MEA long-term durability are under current investigation and will be reported on in follow-up papers.

4. CONCLUSIONS

In summary, we have designed and synthesized a group of low-Pd-loading Pd-Co nanoparticles embedded in a Zn-Co BMOF-derived highly porous carbon support by a facile preparation method. The optimized annealing temperature was found to be 300-400 °C, and the optimized composition was Pd₃Co. Such a catalyst displayed enhanced activity and robust stability for the ORR in alkaline media. The remarkable performance was attributed to the uniform distribution of Pd and Co on the nanoparticles, as confirmed by STEM and EDX mapping, as well as the coexistence of Co-N-C, which helped accelerate the kinetics of the ORR and added additional activity to the BMOF-derived Pd₃Co catalyst. The performance of BMOF-derived Pd₃Co in AEMFCs reached a promising peak power density of 1.1 W/cm² at an ultralow Pd loading of 0.04 mg_{Pd}/cm². This work may provide promising insights into the rational design and optimization of electrocatalysts for fuel cell applications in alkaline media.

ASSOCIATED CONTENT

Supporting Information

The Supporting Information is available free of charge at https://pubs.acs.org/doi/10.1021/acsami.2c10074.

Figures S1-S24 and Tables S1-S3, including additional XRD data, S/TEM images, and electrochemical performance data (PDF)

AUTHOR INFORMATION

Corresponding Author

Héctor D. Abruña - Department of Chemistry and Chemical Biology, Cornell University, Ithaca, New York 14853, United States; orcid.org/0000-0002-3948-356X; Email: hda1@ cornell.edu

Authors

Weixuan Xu - Department of Chemistry and Chemical Biology, Cornell University, Ithaca, New York 14853, United States

Dasol Yoon – Department of Materials Science and Engineering, Cornell University, Ithaca, New York 14853, *United States;* orcid.org/0000-0003-2284-7010

Yao Yang - Department of Chemistry and Chemical Biology, Cornell University, Ithaca, New York 14853, United States; orcid.org/0000-0003-0321-3792

- Yin Xiong Department of Chemistry and Chemical Biology, Cornell University, Ithaca, New York 14853, United States; orcid.org/0000-0002-8560-0894
- Huiqi Li Department of Chemistry and Chemical Biology,Cornell University, Ithaca, New York 14853, United States
- Rui Zeng Department of Chemistry and Chemical Biology, Cornell University, Ithaca, New York 14853, United States; orcid.org/0000-0002-7577-767X
- David A. Muller School of Applied and Engineering Physics, Cornell University, Ithaca, New York 14853, United States; orcid.org/0000-0003-4129-0473

Complete contact information is available at: https://pubs.acs.org/10.1021/acsami.2c10074

Notes

The authors declare no competing financial interest.

ACKNOWLEDGMENTS

This work was supported by the Center for Alkaline-Based Energy Solutions (CABES), part of the Energy Frontier Research Center (EFRC) program supported by the U.S. Department of Energy, under Grant DE-SC-0019445. This work made use of TEM facilities at the Cornell Center for Materials Research (CCMR), which were supported through the National Science Foundation Materials Research Science and Engineering Center (NSF MRSEC) program (DMR-1719875). The authors greatly appreciated the assistance of Qihao Li in the DRT analysis.

REFERENCES

- (1) Chu, S.; Majumdar, A. Opportunities and Challenges for a Sustainable Energy Future. *Nature* **2012**, 488, 294–303.
- (2) Debe, M. K. Electrocatalyst Approaches and Challenges for Automotive Fuel Cells. *Nature* **2012**, 486, 43–51.
- (3) Dunn, B.; Kamath, H.; Tarascon, J. M. Electrical Energy Storage for the Grid: A Battery of Choices. *Science* **2011**, 334, 928–935.
- (4) Gasteiger, H. A.; Markovic, N. M. Just a Dream or Future Reality? *Science* **2009**, 324, 48–49.
- (5) Xiong, Y.; Yang, Y.; Joress, H.; Padgett, E.; Gupta, U.; Yarlagadda, V.; Agyeman-Budu, D. N.; Huang, X.; Moylan, T. E.; Zeng, R.; Kongkanand, A.; Escobedo, F. A.; Brock, J. D.; DiSalvo, F. J.; Muller, D. A.; Abruña, H. D. Revealing the Atomic Ordering of Binary Intermetallics Using in Situ Heating Techniques at Multilength Scales. *Proc. Natl. Acad. Sci. U.S.A* 2019, *116*, 1974—1983.
- (6) Xiong, Y.; Xiao, L.; Yang, Y.; Disalvo, F. J.; Abruña, H. D. High-Loading Intermetallic Pt3Co/C Core-Shell Nanoparticles as Enhanced Activity Electrocatalysts toward the Oxygen Reduction Reaction (ORR). *Chem. Mater.* **2018**, *30*, 1532–1539.
- (7) Stamenkovic, V. R.; Strmcnik, D.; Lopes, P. P.; Markovic, N. M. Energy and Fuels from Electrochemical Interfaces. *Nat. Mater.* **2017**, *16*, 57–69.
- (8) Gasteiger, H. A.; Kocha, S. S.; Sompalli, B.; Wagner, F. T. Activity Benchmarks and Requirements for Pt, Pt-Alloy, and Non-Pt Oxygen Reduction Catalysts for PEMFCs. *Appl. Catal., B* **2005**, *56*, 9–35.
- (9) Wang, D.; Xin, H. L.; Hovden, R.; Wang, H.; Yu, Y.; Muller, D. A.; Disalvo, F. J.; Abruña, H. D. Structurally Ordered Intermetallic Platinum-Cobalt Core-Shell Nanoparticles with Enhanced Activity and Stability as Oxygen Reduction Electrocatalysts. *Nat. Mater.* **2013**, *12*, 81–87.
- (10) Wang, Y. J.; Zhao, N.; Fang, B.; Li, H.; Bi, X. T.; Wang, H. Carbon-Supported Pt-Based Alloy Electrocatalysts for the Oxygen Reduction Reaction in Polymer Electrolyte Membrane Fuel Cells: Particle Size, Shape, and Composition Manipulation and Their Impact to Activity. *Chem. Rev.* **2015**, *115*, 3433–3467.

- (11) Wang, Y.; Yang, Y.; Jia, S.; Wang, X.; Lyu, K.; Peng, Y.; Zheng, H.; Wei, X.; Ren, H.; Xiao, L.; Wang, J.; Muller, D. A.; Abruña, H. D.; Hwang, B. J.; Lu, J.; Zhuang, L. Synergistic Mn-Co Catalyst Outperforms Pt on High-Rate Oxygen Reduction for Alkaline Polymer Electrolyte Fuel Cells. *Nat. Commun.* **2019**, *10*, No. 1509.
- (12) Lu, S.; Pan, J.; Huang, A.; Zhuang, L.; Lu, J. Alkaline Polymer Electrolyte Fuel Cells Completely Free from Noble Metal Catalysts. *Proc. Natl. Acad. Sci. U.S.A* **2008**, *105*, 20611.
- (13) Yang, Y.; Xiong, Y.; Zeng, R.; Lu, X.; Krumov, M.; Huang, X.; Xu, W.; Wang, H.; Disalvo, F. J.; Brock, J. D.; Muller, D. A.; Abruña, H. D. Operando Methods in Electrocatalysis. *ACS Catal.* **2021**, *11*, 1136–1178.
- (14) Ge, X.; Sumboja, A.; Wuu, D.; An, T.; Li, B.; Goh, F. W. T.; Hor, T. S. A.; Zong, Y.; Liu, Z. Oxygen Reduction in Alkaline Media: From Mechanisms to Recent Advances of Catalysts. *ACS Catal.* **2015**, *5*, 4643–4667.
- (15) Zamora Zeledón, J. A.; Stevens, M. B.; Gunasooriya, G. T. K. K.; Gallo, A.; Landers, A. T.; Kreider, M. E.; Hahn, C.; Nørskov, J. K.; Jaramillo, T. F. Tuning the Electronic Structure of Ag-Pd Alloys to Enhance Performance for Alkaline Oxygen Reduction. *Nat. Commun.* **2021**, *12*, No. 620.
- (16) Lu, X.; Ahmadi, M.; Disalvo, F. J.; Abruña, H. D. Enhancing the Electrocatalytic Activity of Pd/M (M = Ni, Mn) Nanoparticles for the Oxygen Reduction Reaction in Alkaline Media through Electrochemical Dealloying. *ACS Catal.* **2020**, *10*, 5891–5898.
- (17) Yang, Y.; Chen, G.; Zeng, R.; Villarino, A. M.; Disalvo, F. J.; van Dover, R. B.; Abruña, H. D. Combinatorial Studies of Palladium-Based Oxygen Reduction Electrocatalysts for Alkaline Fuel Cells. *J. Am. Chem. Soc.* **2020**, *142*, 3980–3988.
- (18) Zhao, Q.; Yan, Z.; Chen, C.; Chen, J. Spinels: Controlled Preparation, Oxygen Reduction/Evolution Reaction Application, and Beyond. *Chem. Rev.* **2017**, *117*, 10121–10211.
- (19) Yang, Y.; Xiong, Y.; Holtz, M. E.; Feng, X.; Zeng, R.; Chen, G.; DiSalvo, F. J.; Muller, D. A.; Abruña, H. D. Octahedral Spinel Electrocatalysts for Alkaline Fuel Cells. *Proc. Natl. Acad. Sci. U.S.A.* **2019**, *116*, 24425–24432.
- (20) Yang, Y.; Zeng, R.; Paik, H.; Kuo, D. Y.; Schlom, D. G.; Disalvo, F. J.; Muller, D. A.; Suntivich, J.; Abruña, H. D. Epitaxial Thin-Film Spinel Oxides as Oxygen Reduction Electrocatalysts in Alkaline Media. *Chem. Mater.* **2021**, 33, 4006–4013.
- (21) Miura, A.; Rosero-Navarro, C.; Masubuchi, Y.; Higuchi, M.; Kikkawa, S.; Tadanaga, K. Nitrogen-Rich Manganese Oxynitrides with Enhanced Catalytic Activity in the Oxygen Reduction Reaction. *Angew. Chem.* **2016**, *128*, 8095–8099.
- (22) Yuan, Y.; Wang, J.; Adimi, S.; Shen, H.; Thomas, T.; Ma, R.; Attfield, J. P.; Yang, M. Zirconium Nitride Catalysts Surpass Platinum for Oxygen Reduction. *Nat. Mater.* **2020**, *19*, 282–286.
- (23) Wu, H.; Chen, W. Copper Nitride Nanocubes: Size-Controlled Synthesis and Application as Cathode Catalyst in Alkaline Fuel Cells. *J. Am. Chem. Soc.* **2011**, *133*, 15236–15239.
- (24) Yang, Y.; Zeng, R.; Xiong, Y.; Disalvo, F. J.; Abruña, H. D. Cobalt-Based Nitride-Core Oxide-Shell Oxygen Reduction Electrocatalysts. *J. Am. Chem. Soc.* **2019**, *141*, 19241–19245.
- (25) Aoki, Y.; Takase, K.; Kiuchi, H.; Kowalski, D.; Sato, Y.; Toriumi, H.; Kitano, S.; Habazaki, H. In Situ Activation of a Manganese Perovskite Oxygen Reduction Catalyst in Concentrated Alkaline Media. *J. Am. Chem. Soc.* **2021**, *143*, 6505–6515.
- (26) Yang, G.; Zhu, J.; Yuan, P.; Hu, Y.; Qu, G.; Lu, B. A.; Xue, X.; Yin, H.; Cheng, W.; Cheng, J.; Xu, W.; Li, J.; Hu, J.; Mu, S.; Zhang, J. N. Regulating Fe-Spin State by Atomically Dispersed Mn-N in Fe-N-C Catalysts with High Oxygen Reduction Activity. *Nat. Commun.* **2021**, *12*, No. 1734.
- (27) Lin, L.; Zhu, Q.; Xu, A. W. Noble-Metal-Free Fe-N/C Catalyst for Highly Efficient Oxygen Reduction Reaction under Both Alkaline and Acidic Conditions. *J. Am. Chem. Soc.* **2014**, *136*, 11027–11033.
- (28) Adabi, H.; Shakouri, A.; Ul Hassan, N.; Varcoe, J. R.; Zulevi, B.; Serov, A.; Regalbuto, J. R.; Mustain, W. E. High-Performing Commercial Fe–N–C Cathode Electrocatalyst for Anion-Exchange Membrane Fuel Cells. *Nat. Energy* **2021**, *6*, 834–843.

ı

- (29) Yin, P.; Yao, T.; Wu, Y.; Zheng, L.; Lin, Y.; Liu, W.; Ju, H.; Zhu, J.; Hong, X.; Deng, Z.; Zhou, G.; Wei, S.; Li, Y. Single Cobalt Atoms with Precise N-Coordination as Superior Oxygen Reduction Reaction Catalysts. *Angew. Chem., Int. Ed.* **2016**, *55*, 10800–10805.
- (30) Yang, L.; Zeng, X.; Wang, W.; Cao, D. Recent Progress in MOF-Derived, Heteroatom-Doped Porous Carbons as Highly Efficient Electrocatalysts for Oxygen Reduction Reaction in Fuel Cells. *Adv. Funct. Mater.* **2018**, 28, No. 1704537.
- (31) Wang, X.; Zhou, J.; Fu, H.; Li, W.; Fan, X.; Xin, G.; Zheng, J.; Li, X. MOF Derived Catalysts for Electrochemical Oxygen Reduction. *J. Mater. Chem. A* **2014**, *2*, 14064–14070.
- (32) Li, Y.; Jia, B.; Fan, Y.; Zhu, K.; Li, G.; Su, C. Y. Bimetallic Zeolitic Imidazolite Framework Derived Carbon Nanotubes Embedded with Co Nanoparticles for Efficient Bifunctional Oxygen Electrocatalyst. *Adv. Energy Mater.* **2018**, *8*, No. 1702048.
- (33) Chaikittisilp, W.; Ariga, K.; Yamauchi, Y. A New Family of Carbon Materials: Synthesis of MOF-Derived Nanoporous Carbons and Their Promising Applications. *J. Mater. Chem. A* **2013**, *1*, 14–19.
- (34) Xiong, Y.; Yang, Y.; Disalvo, F. J.; Abruña, H. D. Metal-Organic-Framework-Derived Co-Fe Bimetallic Oxygen Reduction Electrocatalysts for Alkaline Fuel Cells. *J. Am. Chem. Soc.* **2019**, *141*, 10744–10750.
- (35) Zhao, Y.; Yang, L.; Chen, S.; Wang, X.; Ma, Y.; Wu, Q.; Jiang, Y.; Qian, W.; Hu, Z. Can Boron and Nitrogen Co-Doping Improve Oxygen Reduction Reaction Activity of Carbon Nanotubes? *J. Am. Chem. Soc.* 2013, 135, 1201–1204.
- (36) Xia, B. Y.; Yan, Y.; Li, N.; Wu, H.; bin Lou, X. W. D.; Wang, X. A Metal—Organic Framework-Derived Bifunctional Oxygen Electrocatalyst. *Nat. Energy* **2016**, *1*, No. 15006.
- (37) Chen, X.; Wang, N.; Shen, K.; Xie, Y.; Tan, Y.; Li, Y. MOF-Derived Isolated Fe Atoms Implanted in N-Doped 3D Hierarchical Carbon as an Efficient ORR Electrocatalyst in Both Alkaline and Acidic Media. ACS Appl. Mater. Interfaces 2019, 11, 25976–25985.
- (38) Xiong, Y.; Yang, Y.; DiSalvo, F. J.; Abruña, H. D. Synergistic Bimetallic Metallic Organic Framework-Derived Pt-Co Oxygen Reduction Electrocatalysts. ACS Nano 2020, 14, 13069–13080.
- (39) Kirkland, E. J.; Loane, R. F.; Silcox, J. Simulation of Annular Dark Field Stem Images Using a Modified Multislice Method. *Ultramicroscopy* **1987**, *23*, 77–96.
- (40) Cliff, G.; Lorimer, G. W. The Quantitative Analysis of Thin Specimens. J. Microsc. 1975, 103, 203–207.
- (41) Zhong, H.; Luo, Y.; He, S.; Tang, P.; Li, D.; Alonso-Vante, N.; Feng, Y. Electrocatalytic Cobalt Nanoparticles Interacting with Nitrogendoped Carbon Nanotube in Situ Generated from a Metal-Organic Framework for the Oxygen Reduction Reaction. *ACS Appl. Mater. Interfaces* **2017**, *9*, 2541–2549.
- (42) Zhang, M.; Dai, Q.; Zheng, H.; Chen, M.; Dai, L. Novel MOF-Derived Co@N-C Bifunctional Catalysts for Highly Efficient Zn-Air Batteries and Water Splitting. *Adv. Mater.* **2018**, *30*, No. 1705431.
- (43) Devi, B.; Jain, A.; Roy, B.; Rao, B. R.; Tummuru, N. R.; Halder, A.; Rani Koner, R. Cobalt-Embedded N-Doped Carbon Nanostructures for Oxygen Reduction and Supercapacitor Applications. *ACS Appl. Nano Mater* **2020**, *3*, 6354–6366.
- (44) Yang, Y.; Peng, H.; Xiong, Y.; Li, Q.; Lu, J.; Xiao, L.; Disalvo, F. J.; Zhuang, L.; Abruña, H. D. High-Loading Composition-Tolerant Co-Mn Spinel Oxides with Performance beyond 1 W/cm² in Alkaline Polymer Electrolyte Fuel Cells. ACS Energy Lett. 2019, 4, 1251–1257.
- (45) Hu, M.; Li, Q.; Peng, H.; Ma, H.; Xiao, L.; Wang, G.; Lu, J.; Zhuang, L. Alkaline Polymer Electrolyte Fuel Cells without Anode Humidification and H₂ Emission. *J. Power Sources* **2020**, 472, No. 228471.
- (46) Omasta, T. J.; Park, A. M.; Lamanna, J. M.; Zhang, Y.; Peng, X.; Wang, L.; Jacobson, D. L.; Varcoe, J. R.; Hussey, D. S.; Pivovar, B. S.; Mustain, W. E. Beyond Catalysis and Membranes: Visualizing and Solving the Challenge of Electrode Water Accumulation and Flooding in AEMFCs. *Energy Environ. Sci.* **2018**, *11*, 551–558.
- (47) Hussaini, I. S.; Wang, C. Y. Visualization and Quantification of Cathode Channel Flooding in PEM Fuel Cells. *J. Power Sources* **2009**, 187, 444–451.

- (48) Wan, T. H.; Saccoccio, M.; Chen, C.; Ciucci, F. Influence of the Discretization Methods on the Distribution of Relaxation Times Deconvolution: Implementing Radial Basis Functions with DRTtools. *Electrochim. Acta* **2015**, *184*, 483–499.
- (49) Weiß, A.; Schindler, S.; Galbiati, S.; Danzer, M. A.; Zeis, R. Distribution of Relaxation Times Analysis of High-Temperature PEM Fuel Cell Impedance Spectra. *Electrochim. Acta* **2017**, 230, 391–398. (50) Jang, S.; Her, M.; Kim, S.; Jang, J. H.; Chae, J. E.; Choi, J.; Choi, M.; Kim, S. M.; Kim, H. J.; Cho, Y. H.; Sung, Y. E.; Yoo, S. J. Membrane/Electrode Interface Design for Effective Water Management in Alkaline Membrane Fuel Cells. *ACS Appl. Mater. Interfaces* **2019**, 11, 34805–34811.
- (51) Yang, Y.; Peltier, C. R.; Zeng, R.; Schimmenti, R.; Li, Q.; Huang, X.; Yan, Z.; Potsi, G.; Selhorst, R.; Lu, X.; Xu, W.; Tader, M.; Soudackov, Av.; Zhang, H.; Krumov, M.; Murray, E.; Xu, P.; Hitt, J.; Xu, L.; Ko, H. Y.; Ernst, B. G.; Bundschu, C.; Luo, A.; Markovich, D.; Hu, M.; He, C.; Wang, H.; Fang, J.; Distasio, R. A.; Kourkoutis, L. F.; Singer, A.; Noonan, K. J. T.; Xiao, L.; Zhuang, L.; Pivovar, B. S.; Zelenay, P.; Herrero, E.; Feliu, J. M.; Suntivich, J.; Giannelis, E. P.; Hammes-Schiffer, S.; Arias, T.; Mavrikakis, M.; Mallouk, T. E.; Brock, J. D.; Muller, D. A.; Disalvo, F. J.; Coates, G. W.; Abruña, H. D. Electrocatalysis in Alkaline Media and Alkaline Membrane Based Energy Technologies. *Chem. Rev.* 2022, 122, 6117–6321.